Research Article

Formation of cerium oxide hollow spheres and investigation of hollowing mechanism

Xudong Wu[1,2] · Min Wei[1,2] · Shuhui Yu[1] · Jingyu Huang[1,2] · Rong Sun[1] · Ching-Ping Wong[3]

Abstract

Hollow structure materials have found important applications in many fields such as catalysis, energy storage and sensors. A facile and environmentally benign synthesis will favor their applications. Here we prepare a cerium oxide hollow structure with the size of micrometers through a simple one-step hydrothermal method. This process results in the formation of microspheres at 210 °C for only 2 h. Advantages of this method include no template, without surfactant-assistance or subsequent treatment during the synthesizing process. Explanation on the controlled crystal growth and hollowing mechanism via Ostwald Ripening is proposed elaborately based on the detailed experiment and observation. The FESEM images showed that the surface morphology of the sphere shell turned from initially smoothness into roughness with the increase of reaction time, relating to dissolution and re-deposition of nanoparticles onto inner and outside of the shell. The hollowing microstructure evolvement was vividly presented by observing samples taken out at different reaction stages, which makes visualization of Oswald ripening process. The prepared Cerium oxide microspheres were used to modify glassy carbon electrode, which acts as a sensor for sensitive determination of environmental hormone catechol (CC), demonstrating superior performance over the solid oxide. This work helps to deeply understand Ostwald ripening from a new perspective.

Keywords Hollow materials · Hydrothermal method · Morphology evolvement · Electrochemical detection

1 Introduction

Micro- and nanoscale hollow materials have attracted growing attention for decades, and various hollow structures [1–5] were prepared in recent years. Hollow materials have shown potential applications such as catalysis [6], energy storage [4, 7],sensor [8], and drug delivery [9],which rely on intrinsic features of hollow structures, such as high surface area, hollow interior space, high stability, low density and good permeability. Therefore, it is necessary to study how to control the crystal structure and morphology in order to give full play to the potential application value of these hollow materials. Generally speaking, the synthesis of hollow materials can be classified into two cases: template and template-free. Template assisted material synthesis may utilize hard templates such as silica [10] ,carbon sphere [11] ,polystyrene [12] and metal oxide [13, 14], or soft templates including emulsion micelles [15] and gas bubbles [16, 17]. However, template synthesis can be time-consuming and expensive, and poor crystallinity materials are often produced during the synthesis process [18]. For example, Titirici et al. reported synthesis of metal oxide

---

Electronic supplementary material The online version of this article (https://doi.org/10.1007/s42452-019-0178-0) contains supplementary material, which is available to authorized users.

✉ Shuhui Yu, yuushu@gmail.com; ✉ Rong Sun, rong.sun@siat.ac.cn | [1]Shenzhen Institute of Advanced Electronic Materials, Shenzhen Institutes of Advanced Technology, Chinese Academy of Sciences, Shenzhen 518055, China. [2]Nano Science and Technology Institute, University of Science and Technology of China, Suzhou 215123, China. [3]School of Materials Science and Engineering, Georgia Institute of Technology, Atlanta, GA 30332, USA.

SN Applied Sciences (2019) 1:170 | https://doi.org/10.1007/s42452-019-0178-0

Received: 20 November 2018 / Accepted: 14 January 2019 / Published online: 19 January 2019

hollow spheres by adopting template method during the hydrothermal treatment. Carbon spheres are formed with metal ions incorporated into the hydrophilic shell and the removal of carbon via calcination yields hollow metal oxide spheres. The process contains multi-steps and produces materials with unsatisfactory crystallinity [11]. In contrast, template free approaches toward the synthesis of hollow structures such as galvanic erosion [19, 20], the Kirkendall effect [21, 22], and inside-out Ostwald ripening [5, 23, 24],come with extraordinary advantages, including time-saving and economical, good reproducibility and high yield. Ostwald ripening, a phenomenon which was first described by Wilhelm Ostwald in 1896, [25] involves the dissolution of small crystals and redeposition of the dissolved species on the surface of large particles, which results in growth of larger domain at the expense of the smaller ones. This phenomenon is thermodynamically controlled because small particles with higher surface energy are unstable. In other words, small partcles with higher surface energy appear to have a higher solubility than the large ones. Ostwald ripening has been widely used to explicate the formation of the hollow interior in a crystal. For instance, Zeng et al. reported for the first time the synthesis of hollow TiO_2 nanospheres based on Ostwald ripening mechanism, including the hydrolysis of TiF_4 under hydrothermal conditions in a high pressure vessel reactor [26]. The experimental process can be described as follows: Firstly, TiF_4 forms amorphous solid TiO_2 microspheres by hydrolysis, which is composed of many small crystallites. Secondly, when the reaction time was prolonged, the ripening process occurs by mass transfer between the solid core and the external chemical solution. Finally, the nanospheres eventually become hollow. The Ostwald ripening mechanism also was utilized to synthesize various metal complexes, such as Cu_2O, SnO_2, ZnS, Sb_2S_2, NiS and SiO_2 [3, 5, 27–30]. The above-mentioned hollow particles can be used in catalysis, lithium and sodium storage.

However, the formation mechanism of these hollow structures was not fully understood. For example, how the matter disappears inside the particle lacks convincing explanation. Direct observation by in situ transmission electron microscopy (TEM) and in situ transmission electron microscopy (X-ray microscopy) is helpful to reveal the mechanism of hollowing, which provide real-time information on crystal structure at different reaction stages [19, 20, 31]. It is observed that Oswald ripening is a dynamic material transfer process. By using in situ TEM, Yu et al. [31]. reported the formation of hollow iron oxide nanorods by decomposition of single crystal β-FeOOH. Unlike previously reported inside-out Ostwald ripening, they proposed a hollowing mechanism termed as "shell-induced Ostwald ripening", which involves the dissolution and redepositioning of small nanoparticles on the inner surface of the shell to produce cavities. Although in situ TEM observation offers convenience to reveal hollowing mechanisms, the details of shell morphology could not be observed clearly in the event of particles size at micrometer. FESEM, which presents clear morphology of particles from nano to micro size, can reveal the evolvement of the whole surface morphology of the micrometer particles taken out at different synthesis stage to enrich Oswald ripening theory from another perspective.

Here, inspired by the Oswald ripening mechanism, we report a new one-step synthesis of CeO_2 hollow microspheres to explore surface morphology evolvement without template, surfactant assistance or subsequent treatment. By focusing on the shell evolvement using FESEM to observe entire particles image, we have concisely depicted a hollowing mechanism that enhances previously reported inside-out Ostwald ripening. In our observations, amorphous cores dissolve and nanoparticles redeposit on the interior surface of the shell while small nanoparticles in solution deposit on the outer shell layer simultaneously, generating the hollow cavity and a dense rough shell. This work explains how matter disappears and where it moves. The direct observation of surface morphology using FESEM makes visualization of the Oswald ripening process. The strategy of synthesis and characterization in this study provides general implications for the microscopic morphological evolution of other hollow metal oxide micro- and nanomaterials.

2 Experimental section

2.1 Materials

The chemicals were obtained from the following sources and used without further purification, which include Cerium(III) nitrate hexahydrate ($Ce(NO_3)_3{\cdot}6H_2O$, 99%, Sigma aldrich); Citric acid ($C_6H_8O_7{\cdot}H_2O$, 99.5%, Shanghai Lingfeng Chemical Co. China); Catechol ($C_6H_6O_2$, 99%, Aladdin); Sodium dihydngen phoshate anhydrous (NaH_2PO_4, 99%, Aladdin); and Sodium phosphate dibasic (Na_2HPO_4, 99%, Aladdin).

2.2 Synthesis of CeO_2 hollow microspheres

In a typical experiment, firstly, $Ce(NO_3)_3{\cdot}6H_2O$ (0.4130 g) and $C_6H_8O_7{\cdot}H_2O$ (0.1000 g)(mole ratio = 2:1) were dissolved in 2 mL deionized water and sonicated for 20 min. The mixture solution was placed into a 20 ml Teflon-lined stainless steel autoclave and heated for 0.5 h, 0.75 h, 1 h, and 2 h at 210 °C respectively. After the autoclave was cooled to room temperature naturally, pale yellow precipitates were collected by centrifugation at 5000 rpm for 3 min and washed three times with distilled water and absolute alcohol respectively, and finally dried under vacuum at room temperature for 8 h.

2.3 Fabrication of the modified electrode

Before modification, the bare glassy carbon electrode (GCE) was polished repeatedly with 6, 1, and 0.05 µm alumina powders. After polishing, in order to clean the electrode surface, it was washed with doubly distilled water, and sonicated in ethanol and doubly distilled water for 5 min. Finally, it was dried under nitrogen atmosphere and ready for use. For comparison, an amount of hollow CeO_2 microspheres and solid CeO_2 was dispersed in 5 wt% of Nafion and methanol (1:2) respectively to obtain colloidal sol and the sol was dripped onto the treated GCE. Then the modified electrode was dried at room temperature and subjected for CV analysis.

2.4 Electrochemical measurements of catechol (CC)

The electrochemical property of the CeO_2 microspheres was measured on a CHI 660E electrochemical workstation (Shanghai, China). A conventional three-electrode cell was used. The glassy carbon electrode (GCE) with 3.0-mm diameter served as the working electrode. A saturated calomel electrode (SCE) and a platinum wire electrode were used as the reference electrode and the counter electrode. N_2 atmosphere was kept during the whole experiments.

2.5 Characterization of CeO_2 microspheres

The compositions of the CeO_2 microspheres were identified by X-ray diffraction (XRD, Bruker D8 advance, Germany) with Cu target radiation (λ = 0.15418 nm), and range of measurement angle is 20–80°. The microstructures were characterized by field emission scanning electron microscopy (FESEM; FEI Nova Nano SEM 450, America) with an accelerated voltage of 5 kV. The X-ray photoelectron spectroscopy (XPS) was analyzed by PHI 1800 XPS system (Al target, λ = 0.834 nm, Japan). The surface area and porosity of the CeO_2 hollow microspheres were investigated by means of Brunauer–Emmett–Teller (BET) analysis and nitrogen adsorption and desorption isotherm at 77 K (ASAP-2020, America).

3 Results and discussion

According to the IUPAC definition, Ostwald ripening refers to the "dissolution of small crystals or sol particles and re-deposition of the dissolved species on the surfaces of larger crystals or sol particles" [32]. During Ostwald ripening, relatively small nanoparticles have a greater migration tendency than the larger ones in solution, which increases the possibility of collision and agglomeration. Therefore, with the increase of reaction temperature, the growth of single crystal nanoparticles is at the expense of smaller ones or agglomerated species in the solution. The dissolution of small nanoparticles and aggregates is driven by their higher chemical potential than that of larger particles [33].

3.1 Microstructure evolution of the CeO_2 microspheres

To investigate the formation process of CeO_2 hollow microspheres, the reaction products after different reaction time are examined in detail with FESEM (Fig. 1). The particle size distribution and the coarsening rate are discussed here with respect to our preparation process of CeO_2 microspheres. Obviously, the samples obtained after hydrothermal treatment of 0.5 h contain a large number of solid microspheres, and the growth rate is fast within such a short time. The shell layer looks smooth and a homogeneous core–shell structure appears (Fig. 1a). When the reaction time was prolonged to 0.75 h, the shell looks a little rough (Fig. 1b). We could see clearly that nanoparticles stemming from solution and interior of microspheres are attached to both the outer and inner sides of the spherical shells (Figure S1), which implies that ripening process is on-going. With the reaction time further extended to 1 h

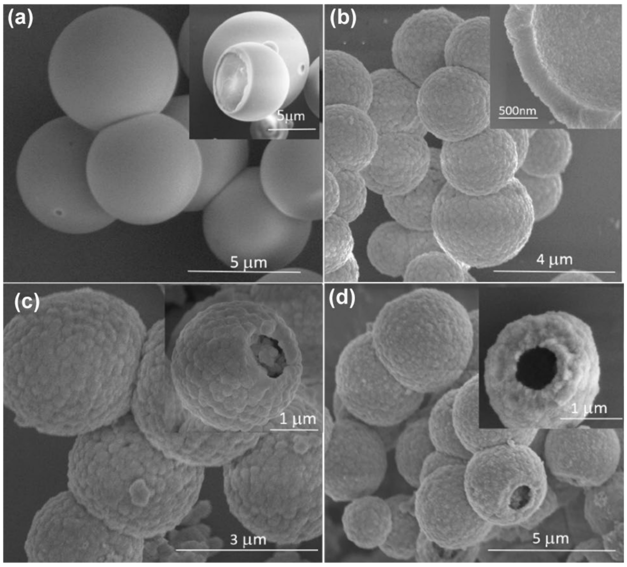

Fig. 1 Field emission scanning electron microscopy (FESEM) images of CeO_2 microspheres obtained at 210 °C after different reaction time of **a** 0.5 h; **b** 0.75 h; **c** 1 h; and **d** 2 h. The insets of a-d show magnified shell structure images corresponding to different reaction time

(Fig. 1c), obvious separation of the center and edge of the microspheres can be observed, and the cavity becomes larger and the shell looks coarser (see also Figure S2). The contrast between the center and the edge indicates that material transfer has happened. After 2 h the inner core is reduced to the minimum value (Fig. 1d) and the shell looks roughest. The shell thickness of the samples after different reaction time measured by FESEM is about 300 nm. Interestingly, compared with the preliminary spheres (Fig. 2a), the spherical size and the shell layer thickness have not changed much during the Ostwald ripening process (Fig. 2b). Eventually, the CeO_2 hollow microspheres are successfully constructed using nano-polyhedron particles as the building blocks which are packed together densely (Fig. 2c, d), meaning that the density of the shell should become high. It has been found that the ripening process does not cease with the extension of reaction time, while the spherical shell becomes very loose and cracks are generated. The shell was composed of a stack of nanoparticles after a reaction time of 5 h (Figure S3). Therefore, the optimal Ostwald ripening time is 2 h.

3.2 Hollowing formation theories of CeO_2 hollow microspheres

Lifshitz Slyozof Wagner (LSW) theory for the first time gave a quantitative description of Ostwald ripening in biphasic systems [34–37]. Based on the LSW theory, some extended theories concerning about dispersed-phase volume fraction, particle movement, different growth mechanisms, and the interactions among crystallites have been developed later [38–44]. The process of Ostwald ripening is a direct consequence of the Kelvin effect [45], and the corresponding equation is given by:

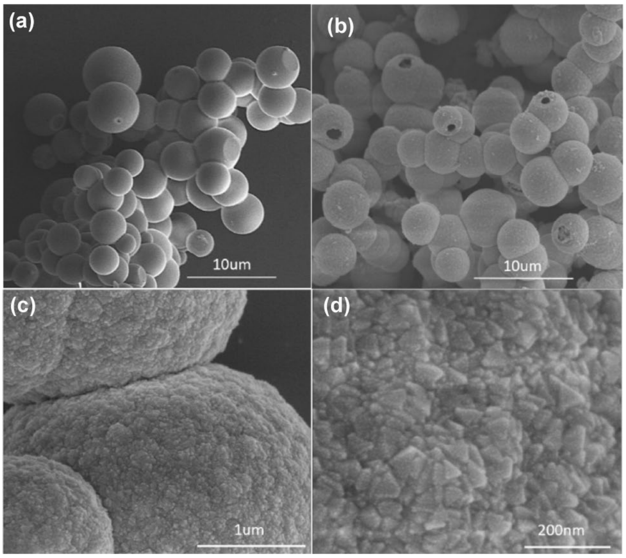

Fig. 2 **a**, **b** Size distribution of the as-prepared microspheres at a reaction time at 210 °C for 0.5 h and 2 h, respectively. **c**, **d** Surface morphology of CeO_2 microspheres at a special reaction time of 2 h

$$C(a) = C(\infty)\exp\left(\alpha/a\right) \tag{1}$$

where C(a)is the solubility of a dispersed phase particle with radius *a*. The bulk solubility C(∞) corresponds to the solubility of a particle with infinite radius, α is called the capillary length and is given by $\alpha = \frac{2\gamma V_m}{RT}$, where *Vm* is the molar volume of the dispersed phase, *γ* is the interfacial tension, *R* is the universal gas constant, and *T* is the absolute temperature. From Eq. (1), it can be seen that small particles are more soluble than large ones. This leads to an increase of average particle size with time. Finsy et al. [44] obtained a class of equations about the Ostwald ripening rate and the particle size distribution. The Ostwald ripening rate *v*, defined as da_N^3/dt, is constant and written as:

$$v = \frac{da_{N^3}}{dt} = \frac{4\alpha D_m C(\infty)}{9} \tag{2}$$

where *Dm* is the molecular diffusion coefficient of the internal phase, and a_N is the number-average particle radius. At any instant of the ripening process, there exists a critical radius a_c. During the ripening process, a_c increases with time. Most coarsening processes exhibit interesting theoretical characteristics because the size distribution of particles does not change with time when the radius equals a_c. This extraordinary behavior is often referred as "self similarity". The particle size distribution can be derived below in the stationary regime, not the transition from an initial situation (freshly prepared dispersion or emulsion) toward the stationary regime.

$$\mathrm{W(a/ac)} = W(\mu) = \frac{81e\mu^2\exp\left(1/(2\mu/3-1)\right)}{\sqrt[3]{32}(\mu+3)^{7/3}(15-\mu)^{11/3}} \tag{3}$$

$$(0 \le \mu \le 1.5)$$

$$W(\mu) = 0(\mu > 1.5)$$

The critical radius a_c is equal to the number-average radius a_N of the limiting self-similar size distribution. Equation (3) implies that no particles with sizes larger than 1.5 times the average size are present in the stationary regime, simultaneously accounts for various particle sizes existing in the hydrothermal system.

Typically, this process (Scheme 1) is illustrated by the initial deposition of amorphous solid microspheres. Although kinetics dominates in the nucleation stage, the polymorphism becomes metastable relative to thermodynamically stable polymorphs as the supersaturation of the surrounding solution decreases with time. Thus, amorphous solids quickly aggregate to form solid smooth spheres to

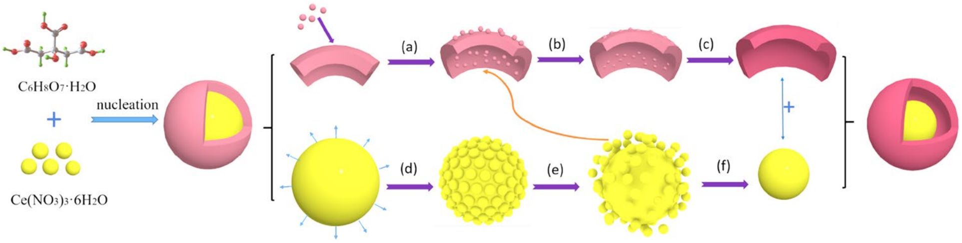

Scheme 1 Proposed mechanism for the synthesis of CeO_2 microspheres in the whole synthetic process. (in order to conveniently describe this process, the part of sphere shell represents the entire one and the yellow sphere represents the spherical core) The hydrothermal treatment of the precursors produced nuclei that formed CeO_2 microspheres. **a** Nanoparticles from solution are attached to the spherical shell. **b** Nanoparticles enter the gap in the spherical shell. **c** Denser shell is generated via mass renormalization. A deeper color represents a larger density. **d** Solubility of interior amorphous agglomerates. **e** The dissolved nanoparticles are attached to the inner surface of the shell. **f** the scale of spherical shell is getting smaller. Finally, the hollow structure is formed with phase coarsening. The shell color becomes darker with the ripening time, indicating denser structure

minimize total energy in the system. Consequently, the newly formed sphere is coated by a thin shell of crystalline phase until the system reaches an equilibrium with the surface shell, which results in density variations between the sphere interior and the shell. Finally, the solid CeO_2 microspheres is divided into two distinct regions to form a core shell structure. As is known, phase transformation must occur on a stable crystal plane so as to maintain uniformity of a crystal structure. The amorphous core keeps in a non-equilibrium state due to its higher solubility compared with the external crystalline layer and as a result, a hollowing effect takes place in the specific region nearest to the shell layer accompanying with the core dissolving. Consequently, the supersaturation of the solution increases, and the secondary nucleation occurs on the inner surface of the shell. As the amorphous core progressively shrinks, the density of the crystalline shell increases, while the thickness of the shell changes little. The continuous dissolution of the core results in decrease of its size, and the spatial distance between the exterior shell and the interior core is gradually enlarged. Eventually, the surface morphology of the sphere shell turned from initially smoothness into roughness. There is no doubt that the relative rates of dissolution and secondary nucleation have a critical bearing on the morphology of the ultimate product. In term of the CeO_2 hollow microspheres product, we could see that the former is relatively slow such that the less crystallized nanoparticles are converted to crystalline ones without complete dissolution (Scheme 1 and Fig. 1). The above statement reveals that Ostwald ripening process takes place through "solid–solution–solid" mass transportation. The smaller and less crystallized precursor nanoparticles inside the solid spheres are transferred out, promoting the morphology transformation from solid to hollow structure. Although the Ostwald ripening process leads to the formation of hollow structures, excessive time will destroy the structure. In order to maintain structural integrity, the optimal reaction time is 2 h. (Scheme 2 and Figure S3)

3.3 XRD and XPS

Powder XRD investigations (Fig. 3) reveals the variation of crystallinity and crystal phase in the whole reaction process. All peaks are readily indexed with JCPDS No. 43-1002, corresponding to cubic fluorite structure of CeO_2. Diffraction peaks of the materials between 2θ values of 69°–80° are weak for the sample at a reaction time of 0.5 h, which indicates that the crystallinity is poor and the degree of disorder is high. The crystallinity of the material increases gradually when the ripening time is prolonged to 2 h, and the morphology of the particles changes significantly due to nucleation and ripening (Fig. 2). This process is related to the gradual redistribution of the matter from the core to the shell of the microspheres. To further investigate the surface composition and the chemical states of the as-prepared materials, XPS analysis were characterized. Peaks of C 1s, O 1s, and Ce 3d can be identified from the survey spectra in Fig. 4a, which indicates the high purity of the sample. Figure 4b displays the Ce 3d spectrum of CeO_2 microspheres, which can be deconvolved into six peaks. The peaks labeled as U_1, V_0, V_1 and U_2, V_2, and V_3 are the characteristic peaks of Ce^{3+} and Ce^{4+} respectively. The

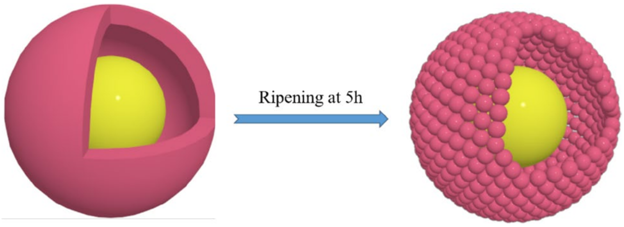

Scheme 2 Shell morphological evolution of CeO_2 microspheres at a reaction stage from 2 to 5 h

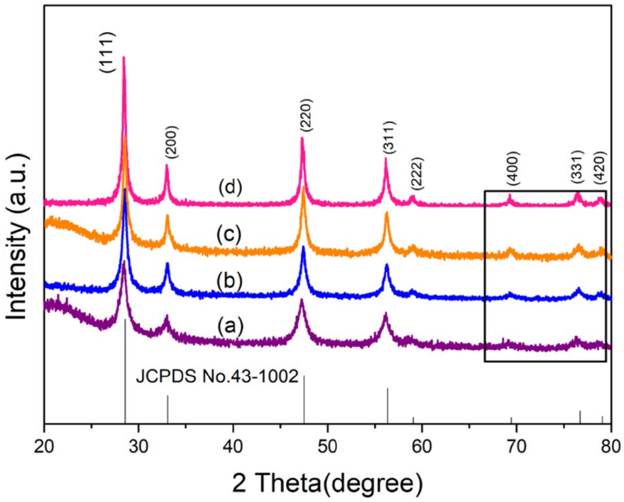

Fig. 3 Powder X-ray diffraction (XRD) patterns of CeO_2 microspheres at different reaction time of **a** 0.5 h; **b** 0.75 h; **c** 1 h; **d** 2 h. The vertical lines represent the diffraction peaks from the standard pattern of JCPDS No. 43-1002

results indicate the co-existence of Ce^{3+} and Ce^{4+} states in CeO_2 microspheres, which is consistent with the previous literature reports [46, 47]. Additionally, The textural porosity of the CeO_2 microspheres were examined by N_2 adsorption and desorption analysis. The results (Figure S4), indicate that the isotherms correspond to type IV and the CeO_2 hollow microspheres sample is a mesoporous material. The corresponding pore size distribution curve calculated by the Barett–Joyner–Halenda (BJH) method using the desorption branch of the isotherm shows the spheres have a narrow pore size distribution from 1 to 10 nm with most pores lying in near 2.5 nm. The surface area of the CeO_2 microspheres with 16.7 m^2/g is higher than the value (8.5 m^2/g) of the commercial CeO_2 powders [48] measured by the Brunauer–Emmett–Teller (BET) method.

3.4 Electrochemical detection of catechol

In the past decades, various analytical techniques such as spectrophotometry, chemiluminescence, chromatography [49–51] have been employed for the detection of catechol (CC) which is an emerging contaminant with severe toxic effects. However, these methods are relatively expensive and time consuming. Remarkably, electrochemical sensors have received considerable attention for environmental monitoring because of their portability, excellent sensitivity, automation, short analysis time, low power consumption and inexpensive equipment [52]. Due to the presence of phenolic hydroxyl groups, CC can be oxidized and exhibit electrochemical activity. We investigated redox activity of the as-obtained CeO_2 hollow microspheres through

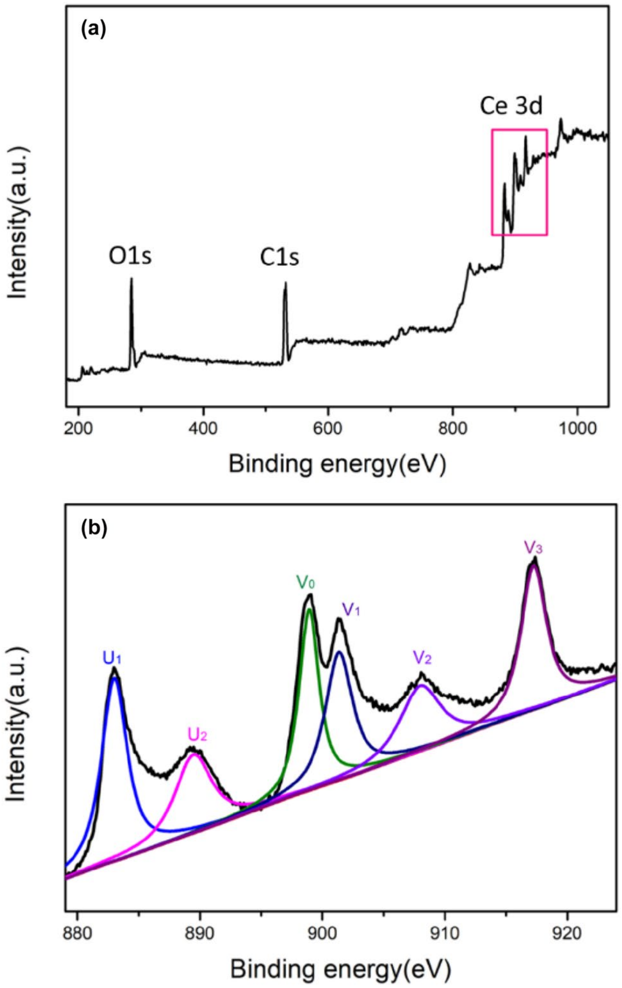

Fig. 4 **a** XPS survey spectrum of CeO_2 hollow microspheres; **b** Ce 3d spectrum of the CeO_2 hollow microspheres

cyclic voltammetry. The CV curves of CeO_2 modified electrode at various scan rates are displayed in Fig. 5a. Both the anodic and cathodic peak currents increase with scan rates. Besides, there is a slight shift in the peaks with increase of the scan rate. In comparison with the solid CeO_2 as shown in Fig. 5b, the hollow CeO_2 microspheres modified electrodes exhibit larger peak current and more negative onset potential, indicating that the hollow CeO_2 microspheres show much better electrocatalysis activity. The formation of mesoporous CeO_2 shells and hollow structure is favorable for the fast diffusion of reactants and products from the active sites, which is beneficial for increasing catalytic efficiency. In Fig. 5c, with the increase of CC concentration from 0.1 to 1.0 mM, the CV curves of CeO_2 microspheres at a scanning rate of 100 mV S^{-1} are given. Obviously, the peak current increases regularly with the addition of CC into the PBS (Phosphate Buffer Solution), showing the stable and reversible electrocatalytic activity of

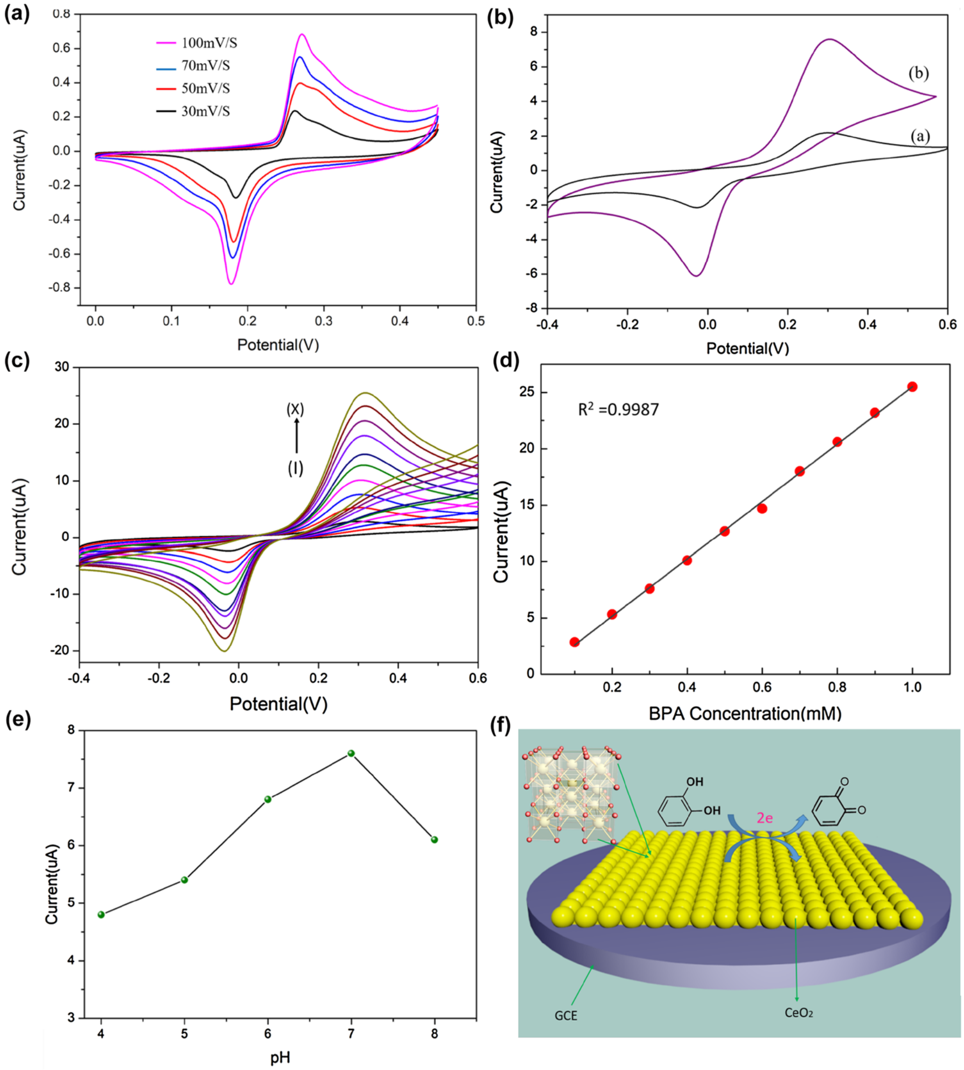

Fig. 5 **a** CV curve of CeO_2 microspheres modified electrode at various scan rates in 0.1 M PBS. **b** CV curves of hollow CeO_2 microspheres (line b) and solid CeO_2 (line a) at a scan rate of 100 mV s^{-1} in 0.3 mM CC. **c** CVs of the obtained hollow CeO_2/GCE electrode towards different concentration of CC (I – X = 0.1,0.2,0.3,0.4,0.5,0.6,0.7,0.8,0.9,1.0 mM) in 0.1 M PBS (pH = 7) at a scanning rate of 100 mV s^{-1}. **d** The calibration plot. **e** CVs of 0.3 mM CC on the CeO_2/GCE at different pH values at a scan rate of 100 mV s^{-1}. **f** A plausible mechanism for the detection of CC by CeO_2 microspheres modified GCE

the CeO_2 microspheres modified GCE. The calibration curve of CeO_2 microspheres modified GCE is shown in Fig. 5d. The linear regression equation is Ip = 0.0646 + 25.438C with the value of correlation coefficient of 0.9987(R^2). The results clearly confirm that the testing process is a diffusion-controlled process. The low detection limit is calculated using the equation [53]: Limit of detection(LOD) = 3Sb/q, where Sb is the standard deviation of the blank signal, and q is the slope of the calibration curve. The calculated LOD is 0.011 mM. The influence of solution pH on the electrocatalytic oxidation of CC at the CeO_2/GCE was investigated by CV in the pH range of 4.0–8.0. As shown in Fig. 5e, the variations in the CV currents at different pH values indicate that the maximum current response can be obtained at pH 7.0. Therefore, 0.1 M PBS with pH 7.0 was used as the supporting electrolyte in all voltammetric determinations. Figure 5f illustrates the possible mechanism for the detection of CC. When CC is oxidized to 1,2-benzoquinone, two free electrons are released, which are absorbed by CeO_2 loaded on the surface of GCE, leading to generation of electric current [54]. This redox behavior demonstrates good electrochemical activity of the prepared CeO_2 microspheres with hollow structure.

4 Conclusion

In summary, we developed a new facial hydrothermal method to prepare uniform CeO_2 microspheres without a template. This process possesses outstanding advantages including time-saving, low cost, good reproducibility and high yield compared with traditional template-directed strategies. The mechanism of controlled growth and hollowing of the microspheres via Ostwald Ripening was proposed elaborately based on the detailed observation. The FESEM images vividly showed the evolution of the surface morphology of the sphere shell. The phase transformation occurred on a stable crystal region (shell layer) so that the uniformity of crystal structure was maintained, which explains clearly how matter disappeared and transferred, to which little attention has been paid in the previous reports. The direct observation of surface morphology evolvement of CeO_2 from a solid core-shell structure to a hollow microsphere with FESEM makes vividly visualization of the Oswald ripening process. The material was electrochemically active and could be explored for more applications like catalysis owing to its prominent redox ability.

Acknowledgements This work was financially supported by the National Natural Science Foundation of China (51777209), Guangdong Provincial Key Laboratory (2014B030301014), and Shenzhen Peacock Program (KQJSCX20170731163718639).

Compliance with ethical standards

Conflicts of interest The authors declare no competing financial interest.

References

1. Xiao Y, Hwang J-Y, Belharouak I, Sun Y-K (2017) Superior Li/Na-storage capability of a carbon-free hierarchical CoSx hollow nanostructure. Nano Energy 32:320–328
2. Liu W, Ma N, Li S, Zhang X, Huo W, Xu J, Meng X, Yang J (2017) A one-step method for pore expansion and enlargement of hollow cavity of hollow periodic mesoporous organosilica spheres. J Mater Sci 52(5):2868–2878
3. Zhang D, Sun W, Zhang Y, Dou Y, Jiang Y, Dou SX (2016) Engineering hierarchical hollow nickel sulfide spheres for high-performance sodium storage. Adv Funct Mater 26(41):7479–7485
4. Zhou L, Zhuang Z, Zhao H, Lin M, Zhao D, Mai L (2017) Intricate hollow structures: controlled synthesis and applications in energy storage and conversion. Adv Mater 29(20):1602914
5. Liu B, Zeng HC (2005) Symmetric and asymmetric Ostwald ripening in the fabrication of homogeneous core-shell semiconductors. Small 1(5):566–571. https://doi.org/10.1002/smll.200500020
6. Prieto G, Tüysüz H, Duyckaerts N, Knossalla J, Wang G-H, Schüth F (2016) Hollow nano-and microstructures as catalysts. Chem Rev 116(22):14056–14119
7. Xie G, Liu X, Li Q, Lin H, Li Y, Nie M, Qin L (2017) The evolution of α-MnO_2 from hollow cubes to hollow spheres and their electrochemical performance for supercapacitors. J Mater Sci 52(18):10915–10926
8. Rao A, Long H, Harley-Trochimczyk A, Pham T, Zettl A, Carraro C, Maboudian R (2017) In situ localized growth of ordered metal oxide hollow sphere array on microheater platform for sensitive, ultra-fast gas sensing. ACS Appl Mater Interfaces 9(3):2634–2641
9. Cao S-W, Zhu Y-J, Ma M-Y, Li L, Zhang L (2008) Hierarchically nanostructured magnetic hollow spheres of Fe_3O_4 and γ-Fe_2O_3: preparation and potential application in drug delivery. J Phys Chem C 112(6):1851–1856
10. Arnal PM, Weidenthaler C, Schüth F (2006) Highly monodisperse zirconia-coated silica spheres and zirconia/silica hollow spheres with remarkable textural properties. Chem Mater 18(11):2733–2739
11. Titirici M-M, Antonietti M, Thomas A (2006) A generalized synthesis of metal oxide hollow spheres using a hydrothermal approach. Chem Mater 18(16):3808–3812
12. Jin Z, Wang F, Wang F, Wang J, Yu JC, Wang J (2013) Metal nanocrystal-embedded hollow mesoporous TiO2 and ZrO2 microspheres prepared with polystyrene nanospheres as carriers and templates. Adv Funct Mater 23(17):2137–2144
13. Mijangos C, Hernández R, Martin J (2016) A review on the progress of polymer nanostructures with modulated morphologies and properties, using nanoporous AAO templates. Prog Polym Sci 54:148–182
14. Lou XW, Yuan C, Archer LA (2007) Double-walled SnO2 nano-cocoons with movable magnetic cores. Adv Mater 19(20):3328–3332
15. He X, Ge X, Liu H, Wang M, Zhang Z (2005) Synthesis of cagelike polymer microspheres with hollow core/porous shell structures by self-assembly of latex particles at the emulsion droplet interface. Chem Mater 17(24):5891–5892
16. Wan J, Stone HA (2011) Coated gas bubbles for the continuous synthesis of hollow inorganic particles. Langmuir 28(1):37–41
17. Wu C, Xie Y, Lei L, Hu S, OuYang C (2006) Synthesis of new-phased VOOH hollow "Dandelions" and their application in lithium–ion batteries. Adv Mater 18(13):1727–1732
18. Yang M, Ma J, Zhang C, Yang Z, Lu Y (2005) General synthetic route toward functional hollow spheres with double-shelled structures. Angew Chem 117(41):6885–6888
19. Shan H, Gao W, Xiong Y, Shi F, Yan Y, Ma Y, Shang W, Tao P, Song C, Deng T (2018) Nanoscale kinetics of asymmetrical corrosion in core-shell nanoparticles. Nat Commun 9(1):1011
20. Chee SW, Tan SF, Baraissov Z, Bosman M, Mirsaidov U (2017) Direct observation of the nanoscale Kirkendall effect during galvanic replacement reactions. Nature Commun 8(1):1224
21. Tianou H, Wang W, Yang X, Cao Z, Kuang Q, Wang Z, Shan Z, Jin M, Yin Y (2017) Inflating hollow nanocrystals through a repeated Kirkendall cavitation process. Nat Commun 8(1):1261
22. Yin Y, Rioux RM, Erdonmez CK, Hughes S, Somorjai GA, Alivisatos AP (2004) Formation of hollow nanocrystals through the nanoscale Kirkendall effect. Science 304(5671):711–714
23. Ma FX, Hu H, Wu HB, Xu CY, Xu Z, Zhen L, Lou XW (2015) Formation of uniform Fe_3O_4 hollow spheres organized by ultrathin nanosheets and their excellent lithium storage properties. Adv Mater 27(27):4097–4101
24. Ding Y, Xia X, Chen W, Hu L, Le Mo, Huang Y, Dai S (2016) Inside-out Ostwald ripening: a facile process towards synthesizing anatase TiO_2 microspheres for high-efficiency dye-sensitized solar cells. Nano Res 9(7):1891–1903
25. Ostwald W (1896) Lehrbuch der Allgemeinen Chemie, vol 2, part 1. Engelmann, Leipzig, Germany. German
26. Yang HG, Zeng HC (2004) Preparation of hollow anatase TiO_2 nanospheres via Ostwald ripening. J Phys Chem B 108(11):3492–3495
27. Chang Y, Teo JJ, Zeng HC (2005) Formation of colloidal CuO nanocrystallites and their spherical aggregation and reductive transformation to hollow Cu_2O nanospheres. Langmuir 21(3):1074–1079
28. Cao X, Gu L, Zhuge L, Gao W, Wang W, Wu S (2006) Template-free preparation of hollow Sb2S3 microspheres as supports for Ag nanoparticles and photocatalytic properties of the constructed metal-semiconductor nanostructures. Adv Funct Mater 16(7):896–902
29. Lou XW, Wang Y, Yuan C, Lee JY, Archer LA (2006) Template-free synthesis of SnO2 hollow nanostructures with high lithium storage capacity. Adv Mater 18(17):2325–2329
30. Wang DP, Zeng HC (2011) Creation of interior space, architecture of shell structure, and encapsulation of functional materials for mesoporous SiO_2 spheres. Chem Mater 23(22):4886–4899

31. Yu L, Han R, Sang X, Liu J, Thomas MP, Hudak BM, Patel A, Page K, Guiton BS (2018) Shell-induced Ostwald ripening: simultaneous structure, composition, and morphology transformations during the creation of hollow iron oxide nanocapsules. ACS Nano 12:9501–9509
32. Alemán J, Chadwick AV, He J, Hess M, Horie K, Jones RG, Kratochvíl P, Meisel I, Mita I, Moad G (2007) Definitions of terms relating to the structure and processing of sols, gels, networks, and inorganic-organic hybrid materials (IUPAC recommendations 2007). Pure Appl Chem 79(10):1801–1829
33. Ali RF, Gates BD (2018) Synthesis of lithium niobate nanocrystals with size focusing through an Ostwald ripening process. Chem Mater 30(6):2028–2035
34. Lifshitz IM, Slyozov VV (1961) The kinetics of precipitation from supersaturated solid solutions. J Phys Chem Solids 19(1–2):35–50
35. Wagner C (1961) Theorie der alterung von niederschlägen durch umlösen (Ostwald-reifung). Zeitschrift für Elektrochemie, Berichte der Bunsengesellschaft für physikalische Chemie 65(7–8):581–591
36. Kabalnov AS, Shchukin ED (1992) Ostwald ripening theory: applications to fluorocarbon emulsion stability. Adv Coll Interface Sci 38:69–97
37. Taylor P (1998) Ostwald ripening in emulsions. Adv Coll Interface Sci 75(2):107–163
38. Ardell A (1972) The effect of volume fraction on particle coarsening: theoretical considerations. Acta Metall 20(1):61–71
39. Brailsford A, Wynblatt P (1979) The dependence of Ostwald ripening kinetics on particle volume fraction. Acta Metall 27(3):489–497
40. Tokuyama M, Kawazaki K (1984) Statistical-mechanical theory of coarsening of spherical droplets. Physica A 123(2–3):386–411
41. Marqusee J, Ross J (1984) Theory of Ostwald ripening: competitive growth and its dependence on volume fraction. J Chem Phys 80(1):536–543
42. Enomoto Y, Tokuyama M, Kawasaki K (1986) Finite volume fraction effects on Ostwald ripening. Acta Metall 34(11):2119–2128
43. Marsh S, Glicksman M (1996) Kinetics of phase coarsening in dense systems. Acta Mater 44(9):3761–3771
44. Finsy R (2004) On the critical radius in Ostwald ripening. Langmuir 20(7):2975–2976
45. Adamson AW, Gast A (1997) Chemistry of Surfaces. Wiley, New York
46. Arul NS, Mangalaraj D, Han JI, Cavalcante LS (2015) Structure and electrochemical detection of xenobiotic micro-pollutant hydroquinone using CeO_2 nanocrystals. Rsc Adv 5(86):70558–70565. https://doi.org/10.1039/c5ra09790h
47. Zhu F, Chen G, Sun S, Sun X (2013) In situ growth of Au@ CeO_2 core–shell nanoparticles and CeO_2 nanotubes from Ce (OH) CO_3 nanorods. J Mater Chem A 1(2):288–294
48. Yang Z, Han D, Ma D, Liang H, Liu L, Yang Y (2009) Fabrication of monodisperse CeO_2 hollow spheres assembled by nano-octahedra. Cryst Growth Des 10(1):291–295
49. Figueiredo EC, Tarley CRT, Kubota LT, Rath S, Arruda MAZ (2007) On-line molecularly imprinted solid phase extraction for the selective spectrophotometric determination of catechol. Microchem J 85(2):290–296
50. Kang J, Li J, Tang J, Li M, Li X, Zhang Y (2010) Sensitized chemiluminescence of Tween 20 on CdTe/H_2O_2 and its analytical applications for determination of phenolic compounds. Colloids Surf, B 76(1):259–264
51. Asan A, Isildak I (2003) Determination of major phenolic compounds in water by reversed-phase liquid chromatography after pre-column derivatization with benzoyl chloride. J Chromatogr A 988(1):145–149
52. Wang F, Yang J, Wu K (2009) Mesoporous silica-based electrochemical sensor for sensitive determination of environmental hormone bisphenol A. Anal Chim Acta 638(1):23–28
53. Mocak J, Bond A, Mitchell S, Scollary G (1997) A statistical overview of standard (IUPAC and ACS) and new procedures for determining the limits of detection and quantification: application to voltammetric and stripping techniques (technical report). Pure Appl Chem 69(2):297–328
54. Sethuraman V, Muthuraja P, Raj JA, Manisankar P (2016) A highly sensitive electrochemical biosensor for catechol using conducting polymer reduced graphene oxide-metal oxide enzyme modified electrode. Biosens Bioelectron 84:112–119. https://doi.org/10.1016/j.bios.2015.12.074